Dirac points embedded in the continuum

Pilar Pujol-Closa and David Artigas*

ICFO - Institut de Ciencies Fotoniques, The Barcelona Institute of Science and Technology and Department of Signal Theory and Communications, Universitat Politècnica de Catalunya, Barcelona 08036, Spain

(Received 14 January 2023; revised 10 October 2023; accepted 16 October 2023; published 3 November 2023)

Hermitian Dirac points play a fundamental role in topological phenomena. The introduction of gain or loss leads to non-Hermitian systems, where Dirac points transform into pairs of exceptional points connected by a Fermi arc. Open non-Hermitian systems also manifest bound states in the continuum (BICs), which are nonradiating resonances located within the band of radiation states. So far, exceptional points have been shown to be robust when interacting with BICs. However, our work unveils that the intersection of two BICs from distinct energy bands along the Fermi arc can prevent the formation of exceptional points, restoring a genuine Hermitian Dirac point instead, albeit surrounded by non-Hermitian states. This represents a different mechanism for the formation of Dirac points embedded in the continuum of radiation, which combines the physics associated to Dirac points and the resonant properties of BICs in non-Hermitian systems. The concept is analyzed using a general model and further explored in a waveguiding photonic system based on hyperbolic dispersion media.

DOI: 10.1103/PhysRevB.108.205106

I. INTRODUCTION

Degeneracy between energy bands has garnered interest since the advent of quantum mechanics [1]. In a Hermitian system, a Dirac point (DP) occurs at the intersection of two dispersion bands, characterized by a conical surface with a linear slope [2–4]. This degenerate state possesses identical eigenvalues and two orthogonal eigenstates, properties that are tightly linked to the conservative character of Hermitian systems. In contrast, non-Hermitian physics delves into systems that lack energy conservation, primarily because energy flows in and out of the Hilbert space under investigation [5]. Recently, the topological concepts and applications of Hermitian systems have been extended to non-Hermitian systems [6–8], with a focus on DPs [9–11]. However, in non-Hermitian systems, the DP gives rise to a pair of exceptional points (EPs) connected by a Fermi arc [12,13]. At the EP, the two bands coalesce and the Hamiltonian is described by a non-diagonal Jordan matrix with identical complex eigenvalues and eigenstates [5]. The band crossing occurs along the Fermi arc, forming two halves of a Riemann surface. Nonorthogonal eigenstates in non-Hermitian systems result in nontrivial dynamics [5,14], including asymmetric mode switching [15,16], topological half charges in polarization states [17], highly sensitive measurements [18,19], and directional lasing and chiral modes [20].

Complex Dirac points can persist in a non-Hermitian system where the DP itself and its neighboring states possess complex eigenvalues, leading to inherent losses [5,11]. Complex DPs, also known as Dirac-like cones, have been identified as crucial elements in achieving zero-index metamaterials in photonic crystal slabs [21,22]. However, the radiation loss associated with these points has hindered their practical applications. To overcome this challenge, a solution was devised by designing a photonic crystal slab in which the complex DP is also a bound state in the continuum (BIC) [23,24]. This approach, referred to as open-Dirac singularity, has recently been employed to demonstrate single-mode laser operation regardless of the cavity size [25].

Eigenstates in non-Hermitian radiative open systems couple to the continuum, thus exhibiting radiation loss. However, BICs are special eigenstates where radiation is suppressed through various mechanisms [26]. BICs exist as confined, lossless states with real eigenvalues and infinite lifetimes, even though they reside within the dispersion band of radiating states that have complex eigenstates and finite lifetimes. While BICs were initially proposed in the context of quantum mechanics [27,28], they are a general wave phenomenon [26] and have been described in diverse physical systems, including acoustics [29], quantum systems [30], and, particularly, photonic platforms [31–35].

In this paper, we demonstrate the formation mechanism of Dirac points embedded in the continuum (DECs) using a generic two-level system. Our findings reveal that DECs arise from the interaction between two BICs residing in different energy bands, which cross at the Fermi arc between EPs. During this process, the EPs can cease to exist, transforming the band structure from a Riemann surface into two conical surfaces that intersect at a single point. At this point, the eigenstates are orthogonal, the eigenvalues are real and degenerate, and the surface slope is linear, resembling a genuine Hermitian DP. However, this DP is surrounded by nonorthogonal eigenstates with complex eigenvalues belonging to the non-Hermitian continuum. We subsequently validate the concept in a photonic system based on hyperbolic waveguides [36–39] with an anisotropic substrate [40,41]. DECs are topological entities potentially capable of retaining all the physics

*david.artigas@icfo.eu

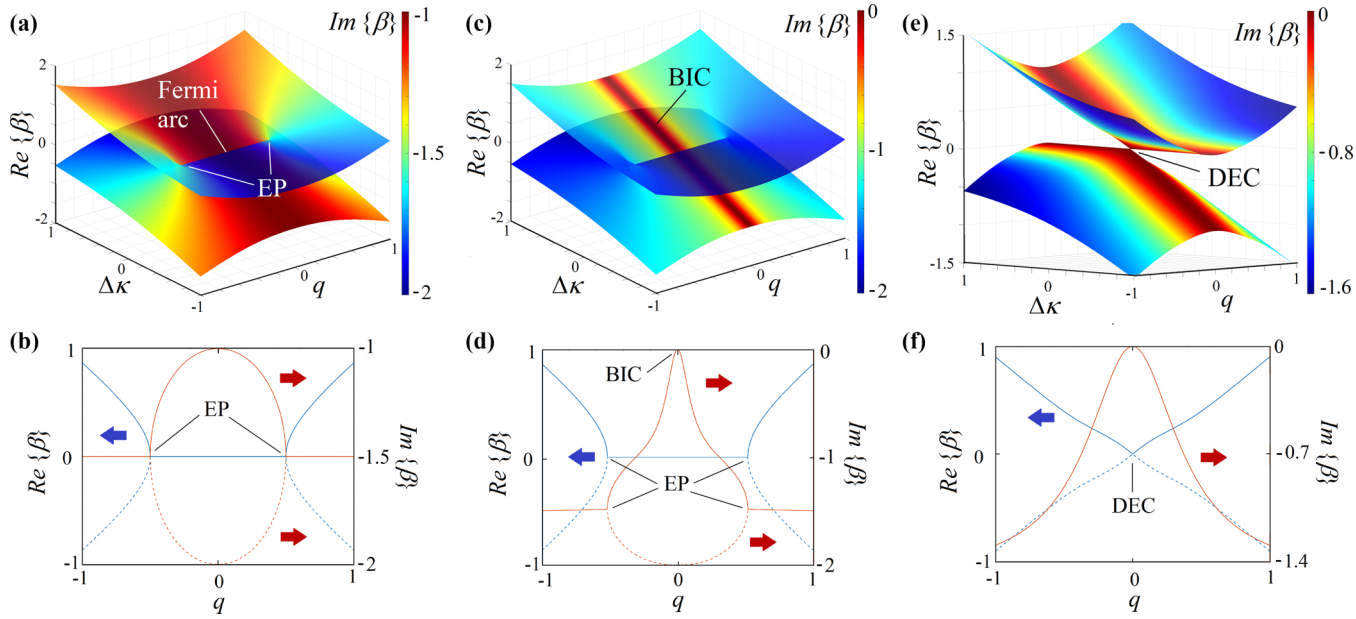

FIG. 1. Eigenvalue bands of a two-level system [Eq. (2)] in terms of the coupling parameter q and the phase mismatch $\Delta\kappa$. $\kappa_1 = -\kappa_2$ with $\alpha_{01} = 1$ and $\alpha_{02} = 2$ in all figures. In (a), $w_1 = w_2 = 0$, so losses remain constant for any value of q and $\Delta\kappa$. In (c), $w_1 = 0.4$ and $w_2 = 0$, so only the E_1 level exhibits a BIC line. In (e), both bands feature a BIC line at $q = 0$, with $w_1 = w_2 = 0.4$, resulting in a DEC. (b), (d), (f) Cuts of the band diagram at $\Delta\kappa = 0$, illustrating the real eigenvalues (blue lines, left y axis) and imaginary eigenvalues (red lines, right y axis) for the cases depicted in (a), (c), (e), respectively. Solid lines represent the upper band, while dashed lines represent the lower band.

associated with DPs (such as topologically protected edge states and backscattering immune transport [42–44]), while also incorporating the resonant properties linked to BICs [45].

II. THE TWO-LEVEL NON-HERMITIAN SYSTEM

The two-level system consists of two coupled resonances with amplitudes E_1 and E_2, which evolve as a function of the parameter z. The dynamics of the system can be described by the momentum, κ_j, the attenuation constant associated with the radiation channel, α_j, and the coupling between the two resonances, q, as [14,15]

$$i\frac{d}{dz}\begin{bmatrix}E_1\\E_2\end{bmatrix} = H\begin{bmatrix}E_1\\E_2\end{bmatrix} = \begin{bmatrix}\kappa_1 - i\alpha_1 & q\\ q & \kappa_2 - i\alpha_2\end{bmatrix}\begin{bmatrix}E_1\\E_2\end{bmatrix}, \quad (1)$$

where H is its Hamiltonian. Equation (1) supports harmonic solutions, $E_j = a_j e^{i\beta_j z}$. The eigenvalue β can be described in terms of the momentum mismatch, $\Delta\kappa = \kappa_2 - \kappa_1$, and the attenuation mismatch, $\Delta\alpha = \alpha_2 - \alpha_1$, as

$$\beta = \left(\kappa_{av} - i\alpha_{av} \pm \tfrac{1}{2}\sqrt{4q^2 + (\Delta\kappa - i\Delta\alpha)^2}\right), \quad (2)$$

where $\kappa_{av} = (\kappa_2 + \kappa_1)/2$ and $\alpha_{av} = (\alpha_2 + \alpha_1)/2$ are the averaged momentum and attenuation constant, respectively. For simplicity, and since κ_{av} only adds an offset to the eigenvalue, we adopt the standard convention of setting $\kappa_{av} = 0$ in our calculations.

Figure 1(a) shows the typical eigenvalue bands of the system as a function of q and $\Delta\kappa$. The EP appears at $\Delta\kappa = 0$ and $q = \Delta\alpha/2$, with eigenvalue $\beta = \kappa_{av} - i\alpha_{av}$. The Fermi arc is observed connecting the two EPs in Fig. 1(a) at $\Delta\kappa = 0$, where both bands intersect with equal $\mathrm{Re}(\beta)$ but different $\mathrm{Im}(\beta)$ [see Fig. 1(b)]. When $\Delta\alpha = 0$, the two EPs collapse at $\Delta\kappa = 0, q = 0$ into a single EP, or complex DP, with one complex eigenstate [11]. Consequently, an attenuation mismatch is needed for the existence of the Fermi arc.

The most common problem in non-Hermitian physics is typically associated with absorption losses or amplification. However, our specific focus is on radiating open systems, which have two important implications. First, as the system in Eq. (1) is non-Hermitian, in this framework, all the eigenvalues provided by Eq. (2) define the radiation continuum. Second, unlike absorption losses, radiation losses are determined by the structural and geometrical parameters of the system. Consequently, the values of α_i can vary with changes in the structural parameters q and $\Delta\kappa$. In certain instances, these changes can lead to the formation of a BIC at a specific energy level within the parameter space where α_i equals zero. Such BICs would exhibit an infinite lifetime or propagation distance. BICs manifest as isolated points within the dispersion band in systems with multiple radiation channels [26,34,45] or as continuous lines in systems with a single radiation channel [40,46–48]. The quality factor Q at a BIC is infinite, exhibiting a scaling rule in its proximity such that $Q \propto \alpha_i^{-1} \propto \kappa^{-2}$ [45]. Assuming a similar behavior for the coupling q, so that $\alpha_i \propto q^2$, and an asymptotic behavior when $q \to \infty$, losses in level i can be locally modeled by an absorption,

$$\alpha_i = \alpha_{0i} q^2 / \left(q^2 + w_i^2\right), \quad (3)$$

where w_i is the width of the BIC resonance in level i, and α_{0i} is the radiation loss far away from the BIC ($q \gg w_i$). Equation (3) defines a BIC at $q = 0$ because $\alpha_i = 0$ leads to $\alpha_{av} = \pm\Delta\alpha$, resulting in $\mathrm{Im}\{\beta_1\} = 0$ in Eq. (2).

BICs and EPs coexist in non-Hermitian systems, interacting to produce phenomena such as position swapping [49],

band exchange at the Fermi arc [48], or ultra-low loss EPs in a dual-BIC scheme [50]. The scenario described in Ref. [48] can be simulated by considering a single BIC in the E_1 resonance, as shown in Fig. 1(c) for $w_1 = 0.1$. In this case, a BIC line intersects the Fermi arc and exchanges dispersion bands, while the positions of the EPs remain relatively unchanged. BICs with broader resonance can impact the positions of EPs, but the EPs themselves do not disappear.

A more intriguing scenario arises when both resonances possess BICs. By tuning the system parameters, these two BICs can coincide at the Fermi arc, resulting in a band exchange. Figure 1(e) illustrates this situation for two BIC lines with equal widths ($w_1 = w_2 = 0.4$). A gap between the two bands opens all along the Fermi arc, except at the crossing between the two BICs. Examining this point reveals the coexistence of two orthogonal eigenstates with identical real eigenvalues, exhibiting a linear slope and a conical surface [Fig. 1(f)]. This point does not represent the merging of two bands into a single EP or complex DP [11], as the eigenvalue is real. It also differs from a non-Hermitian DP where gain and losses are balanced [9], as the radiation losses at the intersection of the two BICs are zero, making the system locally Hermitian. However, the surrounding eigenvalues remain complex and are non-Hermitian. Therefore, this point possesses the properties of a DP; however, it is located within the parameter space that corresponds to the radiation continuum. In other words, it is a Dirac point embedded in the continuum (DEC). The existence of DECs only requires two BICs with sufficiently broad resonances to prevent the occurrence of EPs. BICs exchanging branches and DECs also appear when the intersecting BICs are points within the dispersion band, as shown in Figs. 2(a) and 2(b), respectively. This resembles the results in Refs. [23,24] and does not depend on the specific form of Eq. (3).

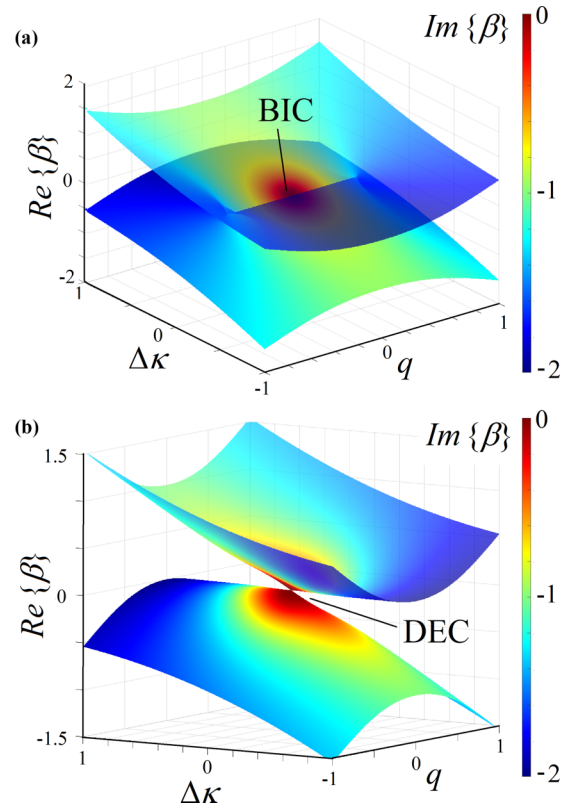

FIG. 2. Eigenvalue bands are depicted in terms of the coupling parameter q and the phase mismatch $\Delta\kappa$. (a) In level E_1, a BIC point occurs at the Fermi arc ($q = 0$ and $\Delta\kappa = 0$) with a width resonance of $w_1 = 0.1$ and $\alpha_{01} = 1$. In level E_2, radiation losses remain constant regardless of q and $\Delta\kappa$, with $\alpha_{02} = 2$ and $w_2 = 0$, resulting in $\Delta\alpha = 1$ when q, $\Delta\kappa \gg w_1$. The result shows how the BIC exchanges bands. (b) A BIC point is present in each energy level for $q = 0$ and $\Delta\kappa = 0$, with a width resonance $w_1 = 0.4$, resulting in a DEC.

III. THE HYPERBOLIC WAVEGUIDE

To demonstrate the existence of DECs in a specific system, we examine the planar hyperbolic waveguide in Fig. 3(a). This structure resembles experimental setups utilizing hyperbolic natural materials [51]. The waveguide consists of a film with a thickness D, which is a type-II hyperbolic medium with positive extraordinary and negative ordinary permittivity ($\varepsilon_{ef} > 1$, $\varepsilon_{of} < 0$) [39]. The substrate is an elliptical negative birefringent substrate with $\varepsilon_{os} > \varepsilon_{es} > 1$. The cladding is air ($\varepsilon_c \geqslant 1$). Each medium is characterized by a diagonal permittivity tensor given by $\hat{\epsilon} = \mathrm{diag}(\epsilon_o, \epsilon_o, \epsilon_e)$. The optical axes (OAs) of the film and substrate are aligned and parallel to the waveguide interfaces. The angle ϕ represents the propagation direction with respect to the OA. Without loss of generality, we assume $\varepsilon_c = 1$, $\varepsilon_{ef} = 1.75^2$, $\varepsilon_{of} = -1.77$, $\varepsilon_{es} = 1.25^2$, and $\varepsilon_{os} = 4$. Nonlocal effects and material absorption are not considered [52]. The boundary condition problem is solved using a transfer matrix method, which is an exact solution of Maxwell's equations (see the Appendix). The method has been further enhanced with analytical routines to improve accuracy[46,53,54], and provides the effective index $N = \beta/k_0$, with $k_0 = 2\pi/\lambda$, which is the eigenvalue in this problem. Figure 3(b) schematically shows the momentum dispersion diagram of the structure, highlighting the regions where various modes with hybrid transverse electric and magnetic (TE/TM) polarization exist. The resonant angle ϕ_{RC} is the asymptotic solution of bulk hyperbolic waves and can be expressed as $\tan\phi_{\mathrm{RC}} = \sqrt{|\varepsilon_{ef}/\varepsilon_{of}|}$. ϕ_{RC} divides the dispersion diagram into four regions. For propagation near the OA [$\phi \in (-\phi_{\mathrm{RC}}, \phi_{\mathrm{RC}})$, green and light-blue regions in the figure], the waveguide supports an infinite number of hybrid but TM-dominant anomalously ordered hyperbolic (TMAH) modes. At higher propagation directions [$\phi \in (\phi_{\mathrm{RC}}, 180^\circ - \phi_{\mathrm{RC}})$, dark-blue and orange regions], a finite number of TE-dominant normally ordered hyperbolic (TENH) modes are supported, along with a hybrid, TM-dominant (TMd) plasmon (for more details, see Ref. [54]). Furthermore, depending on the effective index N, all these modes can be guided modes when $N > n_{os}$ (green and orange regions in the figure) and leaky modes when $n_{es} < \mathrm{Re}\{N\} < \min\{n_{os}, n_{ef}\}$, (dark- and light-blue regions). Leaky modes correspond to improper complex solutions of the eigenmode equation, providing an accurate description of the field near the film. Here, $\mathrm{Re}\{N\}$ gives rise to resonant bands or leaky bands, while $\mathrm{Im}\{N\}$ provides an approximation of the radiation losses. BICs appear

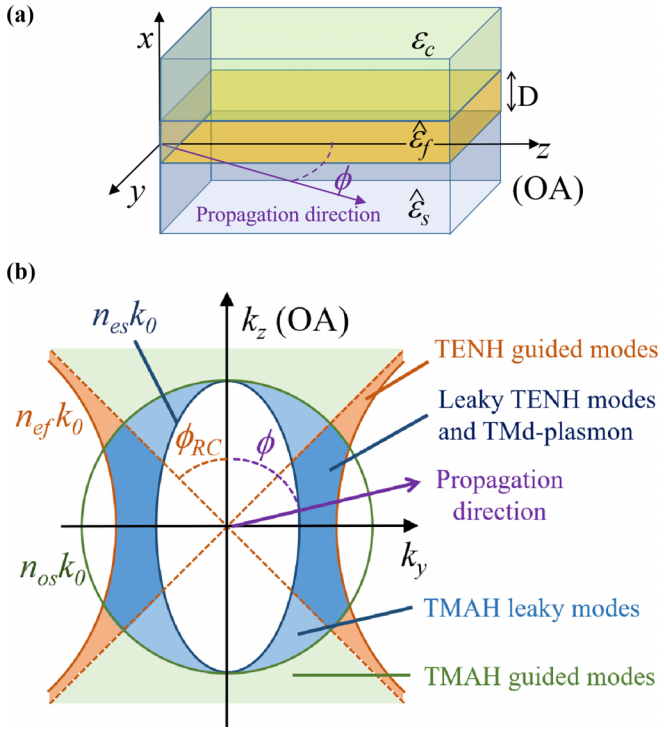

FIG. 3. (a) Waveguide consisting of a hyperbolic film, a negative birefringent substrate, and an isotropic cladding. (b) Scheme of the dispersion diagram showing the modes supported by the structure. The momentum components are given by $k_y = Nk_0 \sin\phi$ and $k_z = Nk_0 \cos\phi$. The ellipsis (blue line) and the circle (green line) correspond to the substrate extraordinary ($n_{es}k_0$) and ordinary ($n_{os}k_0$) bulk momenta. The solid orange line represents the momentum for the extraordinary wave for the bulk hyperbolic material at the film ($n_{ef}k_0$), which approaches the resonant angle ϕ_{RC} asymptotically.

within the leaky bands in the dark-blue region in Fig. 3(b) when $\mathrm{Im}\{N\} = 0$.

According to the previous discussion, hybrid polarized eigenmodes arise due to the coupling between TE and TM modes for any direction ϕ. However, at propagation directions $\phi = 0^\circ$ and 90°, the hybrid modes show pure TE and TM polarization [55]. Therefore, for the present purposes, the mode coupling q can be associated with the propagation direction ϕ. Similarly, the momentum mismatch between modes, $\Delta\kappa$, depends on the normalized film thickness D/λ, where λ represents the free-space wavelength. Thus, the waveguide can be related to the two-level system in Eq. (1), establishing the equivalence $q \Rightarrow \phi$ (with the origin at $\phi = 90^\circ$) and $\Delta\kappa \Rightarrow D/\lambda$, where the eigenvalue in this case corresponds to the effective index $N = \beta/k_0$.

Near $\phi = 90^\circ$, our structure exclusively supports leaky modes. This is shown in the angular dispersion plot in Fig. 4(a). For $D/\lambda < 0.307$, the fundamental mode is a leaky TMd hybrid plasmon, showing both TE and TM components, as demonstrated in Fig. 4(b). The leakage is identified as a nondecaying H_y component at the substrate ($x < 0$), resulting in the radiating channel. As is typical in semi-leaky modes, the TE component is confined. The mode becomes purely TM polarized (absence of an E_y component) at $\phi = 90^\circ$ [Fig. 4(c)]. The effective index at this point is $\mathrm{Re}N = 1.506$, a value that primarily depends on the properties of the film/cladding interface and is minimally affected by variations in D/λ. As N increases with increasing D/λ, bands of the TENH modes emerge from the cutoff. Thus, in contrast to conventional hyperbolic modes, these modes exhibit normal ordering [54], and hence the denomination used in this work. Figure 4(a) shows the first band of these modes, displaying hybrid polarization at $\phi \neq 90^\circ$ [Fig. 4(d)]. As in the TMd band, the H_y component is leaky but exhibits a much lower radiation tail at the substrate. This radiating tail will decrease as the OA orientation approaches the interference BICs (INT-BIC) at $\phi = 77.4^\circ$. At this point, total destructive interference cancels the radiation channel, thus resulting in the INT-BIC. At $\phi = 90^\circ$, the mode becomes pure TE polarized with $N = 1.4054$ [Fig. 4(e)], being a zero-order mode. Note the absence of the TM component, resulting in no radiation and the formation of a polarization-separable BIC (PS-BIC) [40]. This is equivalent to a symmetry-protected BIC in other systems, as the PS-BICs exhibit TE polarization, which is orthogonal to the TM radiation channel.

As the film thickness increases, reaching a value $D/\lambda = 0.307$, the two bands in the dispersion diagram in Fig. 4(f) appear to merge at what seems like a single point. However, upon closer inspection, it becomes evident that there are two EPs joined by a Fermi arc. This becomes more apparent when zooming in on the region of interest and plotting the effective index bands in terms of ϕ and D/λ (Fig. 5). The field amplitudes at the Fermi arc ($\phi = 90^\circ$) show a TE-polarized mode (with a null H_y component) corresponding to a PS-BIC [Fig. 4(g)]. The second solution at the Fermi arc is shown in Fig. 4(h), corresponding to the TM leaky plasmon. In both of these cases, the effective index (eigenstate) of the two eigenmodes falls on the Fermi arc, with the same value of $\mathrm{Re}N = 1.515$, but with different values of $\mathrm{Im}N$. Notably, $\mathrm{Im}N$ is null for the TE-polarized PS-BIC. In contrast, at the EP with $\phi = 90.017^\circ$, as the eigenmode coalesces, there is only one solution with hybrid polarization, containing both TE and TM contributions, as shown in Fig. 4(i).

Consequently, the first TENH_0 mode and the TMd mode intersect at $D/\lambda = 0.307$. The band structure in terms of the propagation direction ϕ (coupling) and D/λ (momentum mismatch) in Fig. 5 shows two EPs connected by a Fermi arc. Similar to Fig. 1(c), the Fermi arc is crossed by a BIC, which in this case corresponds to a PS-BIC. The presence of the BIC does not compromise the existence of the EP; the main effect is the band exchange. Note that at the point $\phi = 90^\circ$ on the Fermi arc, there are two solutions for N: one is real (the BIC) and the other is complex (the TMd plasmon). Therefore, the system exhibits non-Hermitian behavior for all points in Fig. 5.

Another interesting effect occurring at the Fermi arc is the exchange of polarization states. For $D/\lambda < 0.307$, the upper band corresponds to TMd modes and the lower band corresponds to TENH_0 modes, as discussed above in Figs. 4(a)–4(e). However, for $D/\lambda > 0.307$, this order is reversed. This can be observed in the dispersion diagram for $D/\lambda = 0.45$ in Fig. 4(j) and by comparing the field amplitudes at the upper branch in Fig. 4(k), which now corresponds to the TE-polarized PS-BIC with $N = 1.56$, with the field at the lower branch, which now corresponds to the leaky plasmon

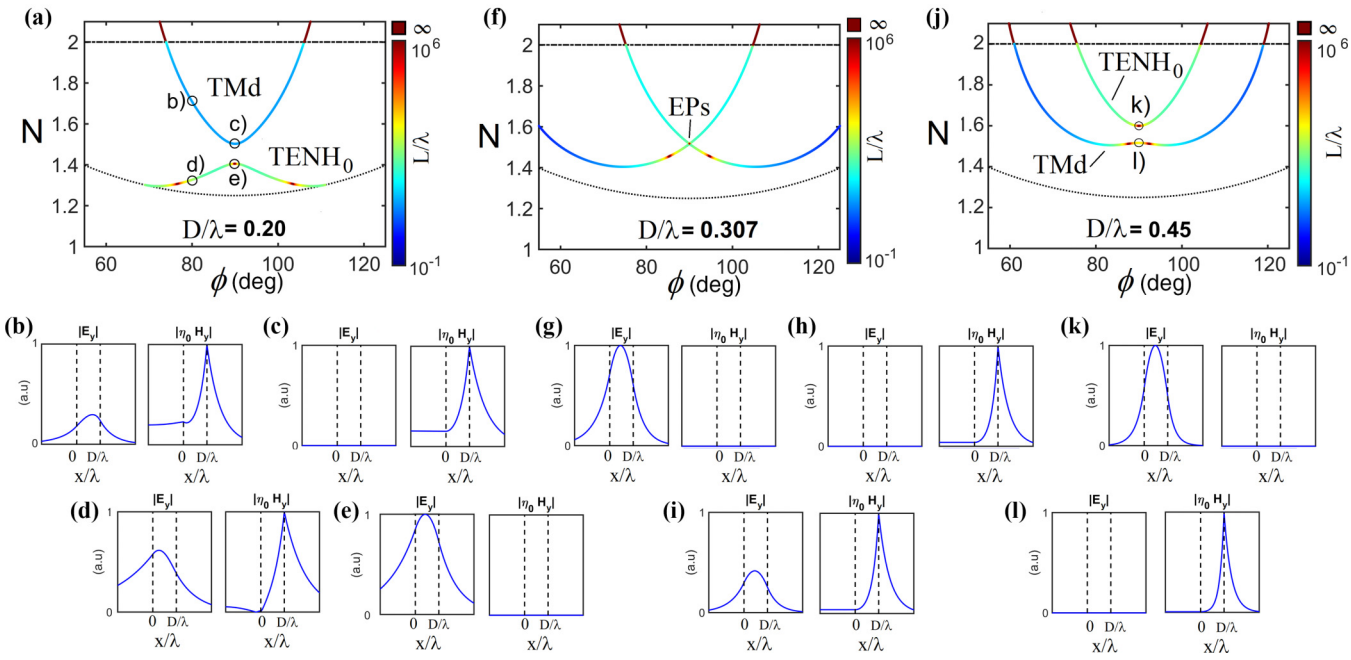

FIG. 4. Angular dispersion diagrams depict bands of mode effective index N as a function of the propagation direction ϕ, along with mode fields corresponding to each band. (a), (f), (j) Dispersion diagrams at $D/\lambda = 0.20$, $D/\lambda = 0.307$, and $D/\lambda = 0.45$, respectively. In these diagrams, the color scale represents the normalized leaky mode propagation length $L = (\mathrm{Im}Nk_0)^{-1}$ relative to λ, with dark red indicating the presence of BICs. The black dotted and dash-dotted lines mark the substrate's extraordinary (n_{es}) and ordinary (n_{os}) refractive indices, respectively. The labels TMd and TENH_0 correspond to the TM-dominant plasmon and the zero-order TE-dominant normally ordered hyperbolic mode, respectively. The labels in (a) indicate the points where field components are plotted for the TMd band, with (b) at $\phi = 80°$ and (c) at $\phi = 90°$. Similarly, for the TENH_0 band, (d) indicates the point at $\phi = 80°$ and in (e) at $\phi = 90°$. (f) A band crossing with two EPs (refer to Fig. 5) near $\phi = 90°$. Field components for the (g) TE and (h) TM eigenmodes at the Fermi arc ($N = 1.515$ and $\phi = 90°$), and (i) at the EP ($\phi = 90.017°$). Labels in (j) indicate points at $\phi = 90°$ where field components are plotted for (k) the TENH_0 and (l) the TMd bands, revealing a mode order exchange between the two bands.

as shown in Fig. 4(l) (all fields are plotted at $\phi = 90°$). This exchange occurs because the TENH_0 band increases $\mathrm{Re}N$ with D/λ, while the TMd band remains almost unchanged with $\mathrm{Re}N = 1.516$ at $\phi = 90°$. In this process of polarization exchange, the TENH_0 band retains the PC-BIC, while the two INT-BICs [red dots in Fig. 4(j)] now belong to the TMd band. The proximity of these two BICs to $\phi = 90°$ results in a significant reduction in radiation losses at this point, and although $\mathrm{Im}N \neq 0$, the leakage is not appreciable in the field profile of the TMd plasmon in Fig. 4(l).

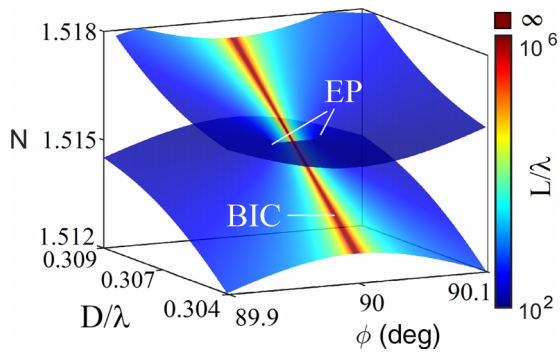

FIG. 5. Effective index bands for the TMd and TENH_0 modes are depicted in terms of ϕ and D/λ. This representation highlights the two EPs and one PS-BIC crossing the Fermi arc. The color scale represents the normalized leaky mode propagation length $L = (\mathrm{Im}Nk_0)^{-1}$ relative to λ.

INT-BICs propagate at values of ϕ that can be adjusted by tuning the waveguide parameters, as demonstrated in the dispersion panels in Fig. 4. Here, it is evident that as D/λ increases, the two INT-BICs on the lower branch approach each other and become closer to $\phi = 90°$. Similarly to previous findings [45], the process of approaching continues until the two INT-BICs merge at $\phi = 90°$, exhibiting a wide region of low losses [see Fig. 6(a)] and forming a single TM-polarized BIC [see Fig. 6(c)]. In addition to the TENH_0 band [see Fig. 6(b)], a new TENH band emerges from the cutoff. The field amplitude examination in Fig. 4(d) reveals that this is a first-order band, i.e., TENH_1, which exhibits a PS-BIC at $\phi = 90°$. The effective index of this new band increases with D/λ. At approximately $D/\lambda \approx 0.88$, the TMd and TENH_1 bands intersect [Fig. 4(e)], and at this intersection point ($\phi = 90°$), both bands feature a BIC. Figure 7 depicts the band structure at the intersection, showcasing a type-II DP [56] at $\phi = 90°$ and $D/\lambda = 0.8804$. At this point, there are two eigenmodes, each showing orthogonal field amplitudes [see Figs. 4(f) and 4(g)], with degenerated eigenvalue N, and, as both fields correspond to BICs, N is real. Therefore, this point is a DEC, exhibiting local Hermiticity and closely resembling the bands depicted in the simpler two-level model of Fig. 1(e). As D/λ increases, the two bands diverge, exchanging polarization characteristics once more [see Figs. 4(i)–4(l)].

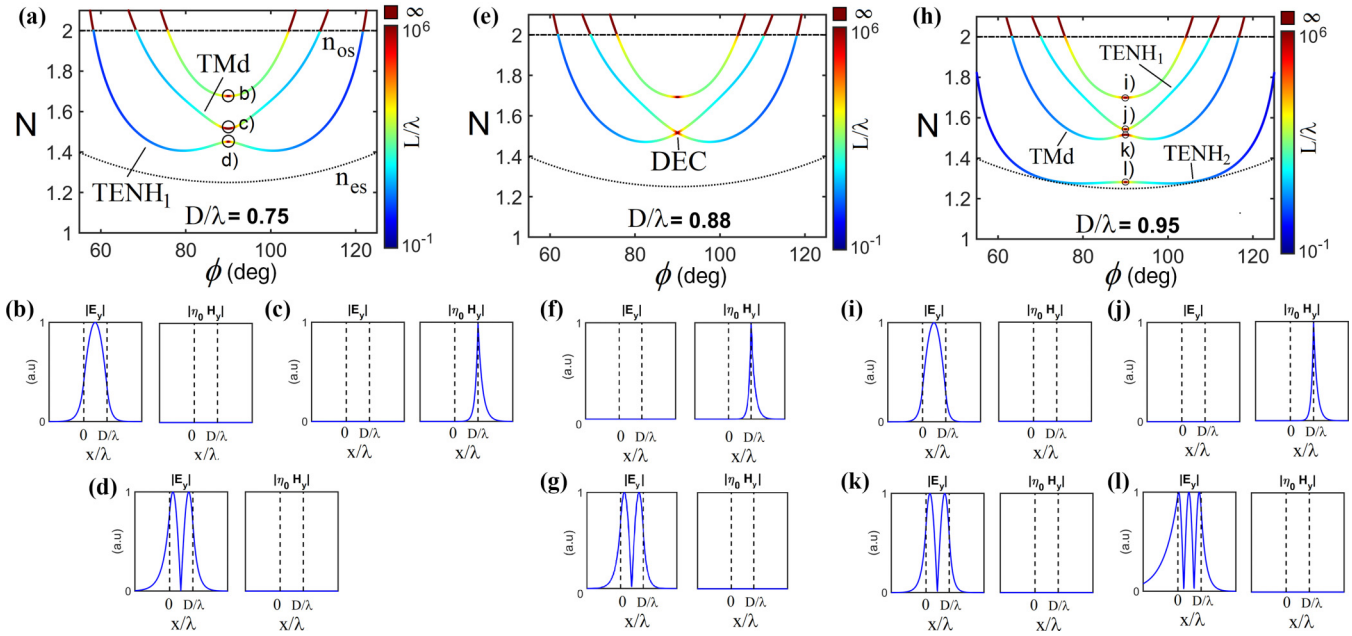

FIG. 6. Same as Fig. 4(a); shows the angular dispersion diagram at $D/\lambda = 0.75$. (b)–(e) The points where the field components are, respectively, plotted in (b) the TENH_0, (c) the TMd, (d) the TENH_1 bands, all of them at $\phi = 90°$. (e) Dispersion diagram at $D/\lambda = 0.88$ displaying the band crossing at the DEC (see Fig. 7). (f), (g) The eigenmode TM and TE field components at the DEC ($N = 1.516$ and $\phi = 90°$). (h) Dispersion diagram at $D/\lambda = 0.95$. (i),(l) The points at $\phi = 90°$ where the field components are, respectively, plotted in (i) the TENH_0, (j) the TENH_1, and (k) the TMd bands, showing mode order exchange between the last two bands. (l) The field components for the newly emerged TENH_2 band. BICs in the dispersion plots appear in red.

The DEC properties were verified through propagation simulation with the finite-difference time-domain (FDTD) method using the MEEP software package [57]. Figure 8(a) shows propagation for both the TENH_1 and TMd orthogonal modes at the DEC, demonstrating that at the DEC, both the TENH_1 and TMd modes are radiationless. However, when the propagation direction is adjusted to $\phi = 80°$, after some initial reshaping of both polarizations, the fields amplitudes exhibit radiation losses directed towards the substrate, in particular the TM component [Fig. 8(b)].

To further validate the concept, we investigate DECs within a cavity consisting of a waveguide section between perfect electric conductors. The length of the cavity is set as $L_c = 2\lambda/N$, where N is chosen for the TENH_1 mode to ensure its resonance within the cavity. The quality factor Q was numerically calculated using the Harminv tool provided by MEEP [57]. The results demonstrate that at the DEC, where both the TENH_1 and TMd modes share the same effective index N, the cavity exhibits a theoretically infinite quality factor (Q) for both the TE and TM components [Fig. 8(c)]. This double resonance is not possible when the cavity is tuned away from the DEC. For example, changing D/λ preserves the BIC nature for both components; however, as the cavity length L_c is optimized for the TENH_1 mode, it exhibits a theoretically infinite Q, while the TMd mode is slightly detuned from resonance, resulting in a lower Q [Fig. 8(d)]. In addition, when ϕ is changed, the supported modes in the cavity are hybrid leaky modes, which display radiation losses. As a consequence, the quality factor Q is significantly reduced, as is the case for $\phi = 85°$ [Fig. 8(d)], where Q has decreased by five orders of magnitude. These results demonstrate that in addition to the spectral resonances provided by the cavity, DECs also offer directional resonance characteristics for both orthogonal polarizations.

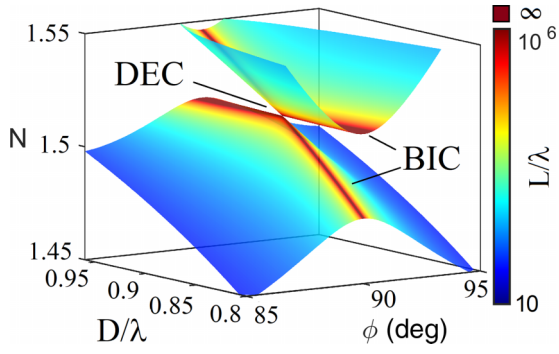

FIG. 7. Same as Fig. 5, but for the TMd and TENH_1 bands, showing the DEC.

IV. DISCUSSION AND CONCLUSIONS

DECs are a topological entity enriching the field of topological physics. DECs occur at the intersection of conical eigenvalue surfaces, featuring a single real eigenvalue and two orthogonal eigenstates. Unlike Hermitian DPs, DECs are Hermitian states surrounded by non-Hermitian states. In contrast to other DPs in non-Hermitian systems, where all states, including the DP, are non-Hermitian [10,11,22] or exhibit PT symmetry [9], DECs are nonradiating states in the presence of radiating states without PT symmetry. In this context, they are similar to open-Dirac singularities [23–25], but with a

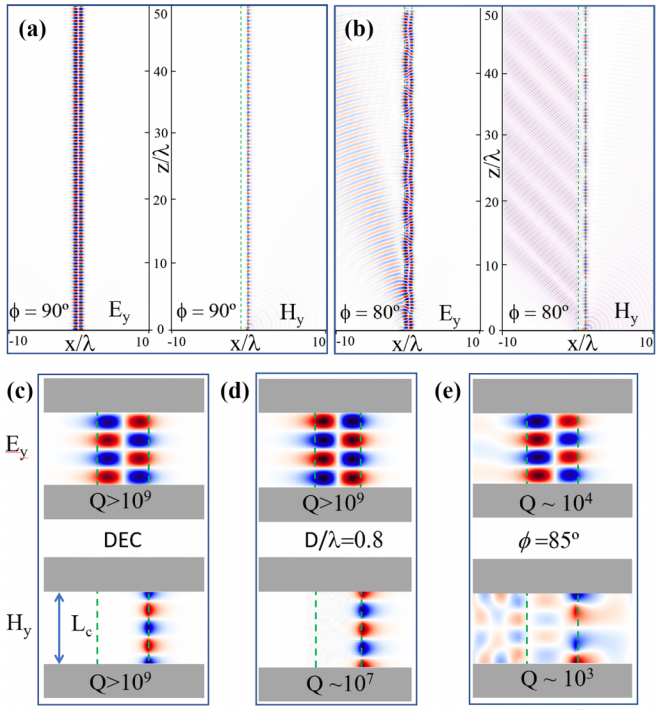

FIG. 8. FDTD simulations showing the electric and magnetic real field amplitudes E_y and H_y. Propagation at (a) the DEC, with propagation direction $\phi = 90^\circ$ and $D/\lambda = 0.8804$, and at (b) for $\phi = 80^\circ$. Cavity simulations for (c) the DEC, (d) $D/\lambda = 0.8$ but keeping $\phi = 90^\circ$, featuring BICs in both branches but outside the DEC, and (e) keeping $D/\lambda = 0.8804$ but with $\phi = 85^\circ$, which do not features BICs. The cavity length in all panels is set to $L_c = 2\lambda/N$, with N corresponding to the TENH_1. This configuration ensures that only the TENH_1 mode is expected to be resonant. The upper row displays the E_y component associated with the TENH_1 mode, while the lower row shows the H_y component associated with the TMd mode. Green dashed lines denote the waveguide interfaces, while the gray areas represent perfect electric conductors.

different origin. Open-Dirac singularities are created from complex DPs [11] that become lossless by synthesizing a BIC at these points, while DECs arise from the interaction of two BICs, preventing the existence of EPs. Compared to standard BICs, DECs exhibit a unique characteristic: a degenerate resonance enabling infinite propagation distances or lifetimes for two orthogonal states. Consequently, the physical properties of DPs in both Hermitian and non-Hermitian systems need to be reexamined in the context of DECs, which could lead to novel forms of electromagnetic and quantum wave state manipulation.

Hyperbolic photonic waveguides provide a suitable platform to put forward the DEC concept. The presence of a hyperbolic film provides a leaky TMd plasmon that can support INT-BICs. As the leaky plasmon is a surface wave, the effective index N remains relatively constant as D/λ increases. This allows for interaction with the successive new leaky TENH_n bands with PS-BICs that emerge from the cutoff, enabling the formation of DECs. In this particular system, the degenerate eigenstates yield a waveguide that exhibits polarization-independent propagation, a characteristic of significance in photonic integrated circuits [58,59]. This attribute is shared with more conventional anisotropic waveguides that possess Dirac points [41]. However, points around the DEC are non-Hermitian, leading to radiation losses. Consequently, lossless propagation exclusively occurs in the direction where the DEC exists, resulting in spatial filtering within the planar waveguide. In a cavity configuration with amplification, this spatial filtering effect could indeed result in collimated lasers, eliminating the need for additional optical elements.

ACKNOWLEDGMENTS

The authors would like to express their gratitude to Dr. Lluís Torner for his insightful comments and for his leadership as the group leader and ICFO Director. This work was supported by Grants No. CEX2019-000910-S, No. PID2022-138280NB-I00, and No. PRE2018-085711 (SEV-2015-0522-18-1) funded by Ministerio de Ciencia e Innovación of Spain, Grant No. MCIN/AEI/10.13039/501100011033/FEDER, Fundació Cellex, Fundació Mir-Puig, and Departament de Recerca i Universitats de la Generalitat de Catalunya (2021 SGR 01448) and CERCA.

APPENDIX: THE TRANSFER MATRIX METHOD

The above modes are calculated using a transfer matrix method. The permittivity tensor for a given layer when the optic axis is aligned in the z direction is given by

$$\hat{\epsilon} = \text{diag}(n_o^2, n_o^2, n_e^2).$$

The optic axis can be reoriented using the appropriate rotation matrix $R_x(\phi)$. The normalized propagation constants in the z direction for the ordinary and extraordinary waves are

$$\kappa_o = \pm\sqrt{n_o^2 - N^2},$$

$$\kappa_e = \pm\sqrt{n_e^2 - N^2\left[\sin^2(\phi) + \left(\frac{n_e^2}{n_o^2}\right)\cos^2(\phi)\right]},$$

where N is the mode effective index. The basis for the field components is given by

$$\overrightarrow{F}_o = \begin{bmatrix} \kappa_o \sin(\phi) \\ n_o^2 \sin(\phi) \\ -\kappa_o \cos(\phi) \\ \kappa_o^2 \cos(\phi) \end{bmatrix}, \quad \overrightarrow{F}_e = \begin{bmatrix} \kappa_o^2 \cos(\phi) \\ \epsilon_o \kappa_e \cos(\phi) \\ \epsilon_o \sin(\phi) \\ -\epsilon_o \kappa_e \sin(\phi) \end{bmatrix},$$

where each element corresponds to the tangential field components E_y, $\eta_0 H_z$, E_z, and $\eta_0 H_y$, respectively, and η_0 is the vacuum impedance. We write the 4×4 field matrix $\hat{F}$ using the Berreman transfer matrix formalism as

$$\hat{F} = \left[\overrightarrow{F_o^+} \ \overrightarrow{F_o^-} \ \overrightarrow{F_e^+} \ \overrightarrow{F_e^-}\right],$$

where the superscript $+(-)$ is the basis waves propagating forward (backward) along x. Then, the total field in a layer in terms of a 4×1 column vector containing the amplitudes $\overrightarrow{a}$

of the respective basis waves is

$$\vec{m} = \hat{F}\vec{a}.$$

The propagation within the same layer separated by a distance D is given by the phase matrix

$$\hat{A}_D = \mathrm{diag}\left(e^{-ik_0\kappa_o^+ D}, e^{-ik_0\kappa_o^- D}, e^{-ik_0\kappa_e^+ D}, e^{-ik_0\kappa_e^- D}\right).$$

Finally, the 4×4 characteristic matrix $\hat{M}$ for a film f of thickness D can be defined as

$$\hat{M} = \hat{F}_f^{-1}\hat{A}_D\hat{F}_f.$$

The cladding and the substrate are semi-infinite and only two (one ordinary and one extraordinary) out of the four basis waves must be selected for these layers.

Guided modes are found when the sign in $\kappa_{o,e}$ is selected to decay exponentially upon moving away from the interfaces for all the polarizations. Leaky modes are selected choosing the sign in $\kappa_{o,e}$ that grows exponentially upon moving away from the interface, but only for the polarization that corresponds to the radiation channel, which in our case is the ordinary wave. Any other polarization is described by evanescent waves.

The fields at the two interfaces at $x = 0$ and $x = D$ are then related using the characteristic matrix $\hat{M}$ as

$$a_o^s \cdot \vec{F}_o^{\,s} + a_e^s \cdot \vec{F}_e^{\,s} = a_o^c \cdot \hat{M}\vec{F}_o^{\,c} + a_e^c \cdot \hat{M}\vec{F}_e^{\,c},$$

where s and c denote the substrate and cladding, respectively, and a_j^i is the amplitude of the corresponding basis wave. Rewriting the previous equation, a homogeneous system of linear equations can be written as

$$\hat{W}\vec{a} = \left[-\hat{M}\vec{F}_o^{\,c} \;\; -\hat{M}\vec{F}_e^{\,c} \;\; \vec{F}_o^{\,s} \;\; \vec{F}_e^{\,s}\right]\vec{a} = 0$$

and the condition for the existence of nontrivial solutions, $|\hat{W}| = 0$, provides the dispersion equation to obtain the values of N for the semi-leaky modes.

[1] C. Herring, Accidental degeneracy in the energy bands of crystals, Phys. Rev. **52**, 365 (1937).

[2] F. D. M. Haldane, Model for a quantum Hall effect without Landau levels: Condensed-matter realization of the "parity anomaly", Phys. Rev. Lett. **61**, 2015 (1988).

[3] A. H. Castro Neto, F. Guinea, N. M. R. Peres, K. S. Novoselov, and A. K. Geim, The electronic properties of graphene, Rev. Mod. Phys. **81**, 109 (2009).

[4] B. Bradlyn, J. Cano, Z. Wang, M. G. Vergniory, C. Felser, R. J. Cava, and B. A. Bernevig, Beyond Dirac and Weyl fermions: Unconventional quasiparticles in conventional crystals, Science **353**, aaf5037 (2016).

[5] Y. Ashida, Z. Gong, and M. Ueda, Non-Hermitian physics, Adv. Phys. **69**, 249 (2020).

[6] D. Leykam, K. Y. Bliokh, C. Huang, Y. D. Chong, and F. Nori, Edge modes, degeneracies, and topological numbers in non-Hermitian systems, Phys. Rev. Lett. **118**, 040401 (2017).

[7] H. Shen, B. Zhen, and L. Fu, Topological band theory for non-Hermitian Hamiltonians, Phys. Rev. Lett. **120**, 146402 (2018).

[8] S. Yao and Z. Wang, Edge states and topological invariants of non-Hermitian systems, Phys. Rev. Lett. **121**, 086803 (2018).

[9] H. Xue, Q. Wang, B. Zhang, and Y. D. Chong, Non-Hermitian Dirac cones, Phys. Rev. Lett. **124**, 236403 (2020).

[10] T. Wang, Special exceptional point acting as Dirac point in one-dimensional symmetric photonic crystal, New J. Phys. **24**, 113016 (2022).

[11] L. Luo, Y. Shao, J. Li, R. Fan, R. Peng, M. Wang, J. Luo, and Y. Lai, Non-Hermitian effective medium theory and complex Dirac-like cones, Opt. Express **29**, 14345 (2021).

[12] B. Zhen, C. W. Hsu, Y. Igarashi, L. Lu, I. Kaminer, A. Pick, S.-L. Chua, J. D. Joannopoulos, and M. Soljai, Spawning rings of exceptional points out of Dirac cones, Nature (London) **525**, 354 (2015).

[13] S. K. Özdemir, Fermi arcs connect topological degeneracies, Science **359**, 995 (2018).

[14] M.-A. Miri and A. Al, Exceptional points in optics and photonics, Science **363**, eaar7709 (2019).

[15] J. Doppler, A. A. Mailybaev, J. Böhm, U. Kuhl, A. Girschik, F. Libisch, T. J. Milburn, P. Rabl, N. Moiseyev, and S. Rotter, Dynamically encircling an exceptional point for asymmetric mode switching, Nature (London) **537**, 76 (2016).

[16] J. W. Yoon, Y. Choi, C. Hahn, G. Kim, S. H. Song, K.-Y. Yang, J. Y. Lee, Y. Kim, C. S. Lee, J. K. Shin, H.-S. Lee, and P. Berini, Time-asymmetric loop around an exceptional point over the full optical communications band, Nature (London) **562**, 86 (2018).

[17] H. Zhou, C. Peng, Y. Yoon, C. W. Hsu, K. A. Nelson, L. Fu, J. D. Joannopoulos, M. Soljai, and B. Zhen, Observation of bulk Fermi arc and polarization half charge from paired exceptional points, Science **359**, 1009 (2018).

[18] H. Hodaei, A. U. Hassan, S. Wittek, H. Garcia-Gracia, R. El-Ganainy, D. N. Christodoulides, and M. Khajavikhan, Enhanced sensitivity at higher-order exceptional points, Nature (London) **548**, 187 (2017).

[19] W. Chen, S. K. Özdemir, G. Zhao, J. Wiersig, and L. Yang, Exceptional points enhance sensing in an optical microcavity, Nature (London) **548**, 192 (2017).

[20] B. Peng, S. K. Özdemir, M. Liertzer, W. Chen, J. Kramer, H. Yılmaz, J. Wiersig, S. Rotter, and L. Yang, Chiral modes and directional lasing at exceptional points, Proc. Natl. Acad. Sci. USA **113**, 6845 (2016).

[21] Y. Li, Y. Wu, X. Chen, and J. Mei, Selection rule for Dirac-like points in two-dimensional dielectric photonic crystals, Opt. Express **21**, 7699 (2013).

[22] Y. Li, C. T. Chan, and E. Mazur, Dirac-like cone-based electromagnetic zero-index metamaterials, Light Sci. Appl. **10**, 203 (2021).

[23] M. Minkov, I. A. D. Williamson, M. Xiao, and S. Fan, Zero-index bound states in the continuum, Phys. Rev. Lett. **121**, 263901 (2018).

[24] H. Tang, C. De Vault, S. A. Camayd-Muoz, Y. Liu, D. Jia, F. Du, O. Mello, D. I. Vulis, Y. Li, and E. Mazur, Low-loss zero-index materials, Nano Lett. **21**, 914 (2021).

[25] R. Contractor, W. Noh, W. Redjem, W. Qarony, E. Martin, S. Dhuey, A. Schwartzberg, and B. Kanté, Scalable

single-mode surface-emitting laser via open-dirac singularities, Nature (London) **608**, 692 (2022).
[26] C. W. Hsu, B. Zhen, A. D. Stone, J. D. Joannopoulos, and M. Soljai, Bound states in the continuum, Nat. Rev. Mater. **1**, 16048 (2016).
[27] J. von Neumann and E. Wigner, Uber merkwürdige diskrete Eigenwerte. Uber das Verhalten von Eigenwerten bei adiabatischen Prozessen, Z. Phys. **30**, 467 (1929).
[28] F. H. Stillinger and D. R. Herrick, Bound states in the continuum, Phys. Rev. A **11**, 446 (1975).
[29] R. Parker, Resonance effects in wake shedding from parallel plates: Some experimental observations, J. Sound Vib. **4**, 62 (1966).
[30] C. S. Kim, A. M. Satanin, Y. S. Joe, and R. M. Cosby, Resonant tunneling in a quantum waveguide: Effect of a finite-size attractive impurity, Phys. Rev. B **60**, 10962 (1999).
[31] D. C. Marinica, A. G. Borisov, and S. V. Shabanov, Bound states in the continuum in photonics, Phys. Rev. Lett. **100**, 183902 (2008).
[32] E. N. Bulgakov and A. F. Sadreev, Bound states in the continuum in photonic waveguides inspired by defects, Phys. Rev. B **78**, 075105 (2008).
[33] Y. Plotnik, O. Peleg, F. Dreisow, M. Heinrich, S. Nolte, A. Szameit, and M. Segev, Experimental observation of optical bound states in the continuum, Phys. Rev. Lett. **107**, 183901 (2011).
[34] C. W. Hsu, B. Zhen, J. Lee, S.-L. Chua, S. G. Johnson, J. D. Joannopoulos, and M. Soljai, Observation of trapped light within the radiation continuum, Nature (London) **499**, 188 (2013).
[35] F. Monticone and A. Alù, Embedded photonic eigenvalues in 3D nanostructures, Phys. Rev. Lett. **112**, 213903 (2014).
[36] D. R. Smith and D. Schurig, Electromagnetic wave propagation in media with indefinite permittivity and permeability tensors, Phys. Rev. Lett. **90**, 077405 (2003).
[37] J. Yao, Z. Liu, Y. Liu, Y. Wang, C. Sun, G. Bartal, A. M. Stacy, and X. Zhang, Optical negative refraction in bulk metamaterials of nanowires, Science **321**, 930 (2008).
[38] M. A. Noginov, Y. A. Barnakov, G. Zhu, T. Tumkur, H. Li, and E. E. Narimanov, Bulk photonic metamaterial with hyperbolic dispersion, Appl. Phys. Lett. **94**, 151105 (2009).
[39] O. Takayama and A. V. Lavrinenko, Optics with hyperbolic materials, J. Opt. Soc. Am. B **36**, F38 (2019).
[40] J. Gomis-Bresco, D. Artigas, and L. Torner, Anisotropy-induced photonic bound states in the continuum, Nat. Photon. **11**, 232 (2017).
[41] J. Gomis-Bresco, D. Artigas, and L. Torner, Transition from Dirac points to exceptional points in anisotropic waveguides, Phys. Rev. Res. **1**, 033010 (2019).
[42] C. L. Kane and E. J. Mele, Quantum spin Hall effect in graphene, Phys. Rev. Lett. **95**, 226801 (2005).
[43] F. D. M. Haldane and S. Raghu, Possible realization of directional optical waveguides in photonic crystals with broken time-reversal symmetry, Phys. Rev. Lett. **100**, 013904 (2008).
[44] T. Ozawa, H. M. Price, A. Amo, N. Goldman, M. Hafezi, L. Lu, M. C. Rechtsman, D. Schuster, J. Simon, O. Zilberberg, and I. Carusotto, Topological photonics, Rev. Mod. Phys. **91**, 015006 (2019).
[45] J. Jin, X. Yin, L. Ni, M. Soljai, B. Zhen, and C. Peng, Topologically enabled ultrahigh-q guided resonances robust to out-of-plane scattering, Nature (London) **574**, 501 (2019).
[46] S. Mukherjee, J. Gomis-Bresco, P. Pujol-Closa, D. Artigas, and L. Torner, Topological properties of bound states in the continuum in geometries with broken anisotropy symmetry, Phys. Rev. A **98**, 063826 (2018).
[47] S. Mukherjee, D. Artigas, and L. Torner, Surface bound states in the continuum in dyakonov structures, Phys. Rev. B **105**, L201406 (2022).
[48] A. Cerjan, C. W. Hsu, and M. C. Rechtsman, Bound states in the continuum through environmental design, Phys. Rev. Lett. **123**, 023902 (2019).
[49] R. Kikkawa, M. Nishida, and Y. Kadoya, Bound states in the continuum and exceptional points in dielectric waveguide equipped with a metal grating, New J. Phys. **22**, 073029 (2020).
[50] H. Qin, X. Shi, and H. Ou, Exceptional points at bound states in the continuum in photonic integrated circuits, Nanophotonics **11**, 4909 (2022).
[51] J. John, A. Slassi, J. Sun, Y. Sun, R. Bachelet, J. Pénuelas, G. Saint-Girons, R. Orobtchouk, S. Ramanathan, A. Calzolari, and S. Cueff, Tunable optical anisotropy in epitaxial phase-change Vo2 thin films, Nanophotonics **11**, 3913 (2022).
[52] M. Mahmoodi, S. H. Tavassoli, O. Takayama, J. Sukham, R. Malureanu, and A. V. Lavrinenko, Existence conditions of high-k modes in finite hyperbolic metamaterials, Laser Photon. Rev. **13**, 1800253 (2019).
[53] S. Mukherjee, J. Gomis-Bresco, P. Pujol-Closa, D. Artigas, and L. Torner, Angular control of anisotropy-induced bound states in the continuum, Opt. Lett. **44**, 5362 (2019).
[54] P. Pujol-Closa, J. Gomis-Bresco, S. Mukherjee, J. S. Gómez-Díaz, L. Torner, and D. Artigas, Slow light mediated by mode topological transitions in hyperbolic waveguides, Opt. Lett. **46**, 58 (2021).
[55] A. Knoesen, T. K. Gaylord, and M. G. Moharam, Hybrid guided modes in uniaxial dielectric planar waveguides, J. Lightwave Technol. **6**, 1083 (1988).
[56] J. Kim, S. Yu, and N. Park, Universal design platform for an extended class of photonic dirac cones, Phys. Rev. Appl. **13**, 044015 (2020).
[57] A. Oskooi, D. Roundy, M. Ibanescu, P. Bermel, J. D. Joannopoulos, and S. G. Johnson, MEEP: A flexible free-software package for electromagnetic simulations by the FDTD method, Comput. Phys. Commun. **181**, 687 (2010).
[58] S. P. Chan, C. E. Png, S. T. Lim, G. T. Reed, and V. M. N. Passaro, Single-mode and polarization-independent silicon-on-insulator waveguides with small cross section, J. Lightwave Technol. **23**, 2103 (2005).
[59] J. Guan, X. Liu, P. S. Salter, and M. J. Booth, Hybrid laser written waveguides in fused silica for low loss and polarization independence, Opt. Express **25**, 4845 (2017).